Check for updates

MEMRISTORS

High-temperature memristors enabled by interfacial engineering

Jian Zhao[1], Cameron S. Jorgensen[2], Krishnamurthy Mahalingam[2], Cynthia Bowers[2], Wataru Sugimoto[3], Kai Ito[3], Seung Ju Kim[1], Ruoyu Zhao[1], Yichun Xu[1], Han-Ting Liao[1], Rajiv K. Kalia[4], Aiichiro Nakano[4], Kohei Shimamura[3], Fuyuki Shimojo[3], Priya Vashishta[4], Ajit K. Roy[2], Ning Ge[5], Miao Hu[5], R. Stanley Williams[1], Qiangfei Xia[5,6], Sabyasachi Ganguli[2], J. Joshua Yang[1,5]*

Nonvolatile memories (NVMs) that operate reliably at high temperatures are essential for electronics in extreme environments. Here, we report graphene (Gra)/HfO_x/tungsten (W) memristors that operated reliably up to 700°C, with an ON/OFF current ratio of $>10^3$, data retention >50 hours, and endurance $>10^9$ switching cycles. Transmission electron microscopy revealed substantial W diffusion into the inert platinum (Pt) electrode in conventional Pt/HfO_x/W memristors after high-temperature annealing, which was responsible for the thermal failure in conventional devices but not observed in Gra/HfO_x/W devices. First-principles calculations attributed the enhanced thermal stability to weaker W adsorption and higher surface diffusion barriers on Gra compared with metals such as Pt. These results underscore the critical role of interfacial engineering and the potential of two-dimensional materials for enabling reliable high-temperature NVM technologies.

Traditional complementary metal-oxide semiconductor (CMOS)–based silicon devices exhibit substantial reliability issues when operating temperature exceeds 200°C (*1*). Although logic transistors based on wide-bandgap semiconductors such as silicon carbide have demonstrated operation at temperatures up to 800°C (*2*), the development of nonvolatile memories (NVMs) capable of reliable data programming and retention above 300°C remains a major challenge (*3*). Nevertheless, applications such as space exploration, deep-well drilling, nuclear energy, and autonomous vehicles require electronic components that remain stable above 500°C (*4*). To meet these demands, new materials must be explored to overcome the inherent thermal limitations of traditional technologies.

In many NVM technologies, data are encoded in the form of resistance in active materials that can reversibly switch between at least two distinct states. Phase-change memories, for example, exploit the transition of chalcogenides such as $Ge_2Sb_2Te_5$ between amorphous and crystalline phases, but the recrystallization occurring near 200°C substantially limits their functionality at high temperatures (*5*, *6*). Flash memory is widely used, but its reliable operation rarely exceeds 200°C, with substantial degradation at higher temperatures (*3*, *4*, *7*–*10*). Ferroelectric memories that use materials with high Curie temperatures and large coercive fields, such as $Al_xSc_{1-x}N$, have shown promise in a recent demonstration, operating at temperatures up to 600°C with 6-hour data retention and a write endurance of 10^3 cycles (*11*). However, practical applications also require devices to exhibit a high ON/OFF current ratio, low switching voltage, and a compact footprint.

Resistive switching (RS) memory is another widely studied NVM technology and shows high potential for energy-efficient edge computing (*12*–*15*). Because RS is governed by ionic migration, higher temperatures substantially increase ion mobility, compromising thermal stability and hastening device degradation. A notable example of high-temperature performance is a type of memristor constructed entirely from layered two-dimensional (2D) materials, specifically Gra/$MoS_{2-x}O_x$/Gra, which have demonstrated stable operation up to 340°C, with 27-hour data retention and a write endurance of 10^3 cycles (*16*). Their thermal robustness is attributed to the preserved atomic-layer structure of both the switching medium ($MoS_{2-x}O_x$) and the Gra electrodes. The strategy of replacing either the active layer or the electrodes with 2D materials has been widely explored to improve room-temperature (RT) performance (*17*–*24*). However, large-scale integration tends to favor fabrication processes that minimize the need for transferring and patterning multiple 2D layers. Moreover, it is advantageous to use RS layers that can be reproducibly prepared with standard foundry processes. Despite these constraints, the findings underscore a promising direction: Combining bulk oxide switching layers with thermally stable 2D electrodes may offer a practical route toward reliable high-temperature memristors.

In this work, we present a new type of bipolar memristor in which the conventional inert platinum (Pt) bottom electrode in Pt/HfO_x/W devices was replaced by a 2D Gra layer, for which wafer-scale synthesis has already been demonstrated (*25*). In addition, W was chosen as the counter electrode because of its superior melting point. HfO_x, a foundry-favored switching material, was adopted as the memristive switching layer. The resulting Gra/HfO_x/W devices exhibited stable operation with an ON/OFF current ratio exceeding three orders of magnitude, consistently maintained from RT up to 700°C. Both ON and OFF states demonstrated data retention for at least 50 hours, and the devices endured more than 10^9 switching cycles at 700°C. Additionally, the devices could be reliably switched by 30-ns-wide voltage pulses from RT to 700°C, with a switching voltage of ~1.5 V at 700°C.

To investigate the origin of this exceptional thermal robustness, we conducted annealing tests on Pt/HfO_x/W control devices. High-resolution transmission electron microscopy (HRTEM), energy-dispersive x-ray spectroscopy (EDS), and electron energy loss spectroscopy (EELS) were used to compare the microstructural evolution of Gra/HfO_x/W and Pt/HfO_x/W devices after annealing at 800°C. First-principles calculations were also performed to study the behavior of W adatoms on Pt and Gra surfaces, providing theoretical understanding of the mechanism underlying the enhanced thermal stability.

Device structure and high-temperature performance

In Fig. 1A, we show a schematic of the Gra/HfO_x/W memristor. Multilayer Gra flakes were mechanically exfoliated and transferred onto Si/SiO_2 substrates. The RS layer was then patterned by use of electron-beam lithography (EBL), followed by radio frequency sputtering of a 7.5-nm HfO_x film [80 W, 20 standard cubic centimeters per minute (SCCM) Ar, 3.5 mtorr] and liftoff. A second EBL step was used to define the electrodes, after which 40 nm W was deposited by means of direct current (dc) sputtering (200 W, 20 SCCM Ar, 3 mtorr), followed by liftoff. To complete the device fabrication, we performed rapid thermal annealing at 600°C for 20 s to promote partial crystallization of the HfO_x layer and eliminate polymer residues at the interface, improving contact quality. The resulting device area, defined by the overlap between the bottom Gra and top W electrodes, ranges from 200 nm by 1 μm to 1 μm by 1 μm (fig. S1A). Elemental mapping using EELS confirmed the spatial distribution of C, Hf, and W elements (fig. S1B).

We evaluated the in situ switching performance of the Gra/HfO_x/W device at elevated temperatures. In Fig. 1B, we present the bipolar quasi-dc current-voltage (*I*-*V*) characteristics of a representative device measured from RT to 700°C under a vacuum of $\sim 1 \times 10^{-4}$ torr. We demonstrate in movie s1 in situ dc switching over multiple continuous

[1]Department of Electrical and Computer Engineering, University of Southern California, Los Angeles, CA, USA. [2]Airforce Research Lab/RX, Dayton, OH, USA. [3]Department of Physics, Kumamoto University, Kumamoto, Japan. [4]Collaboratory for Advanced Computing and Simulation, University of Southern California, Los Angeles, CA, USA. [5]TetraMem, Fremont, CA, USA. [6]Department of Electrical and Computer Engineering, University of Massachusetts, Amherst, MA, USA. *Corresponding author. Email: jjoshuay@usc.edu

Downloaded from https://www.science.org at University of Southern California on May 22, 2026

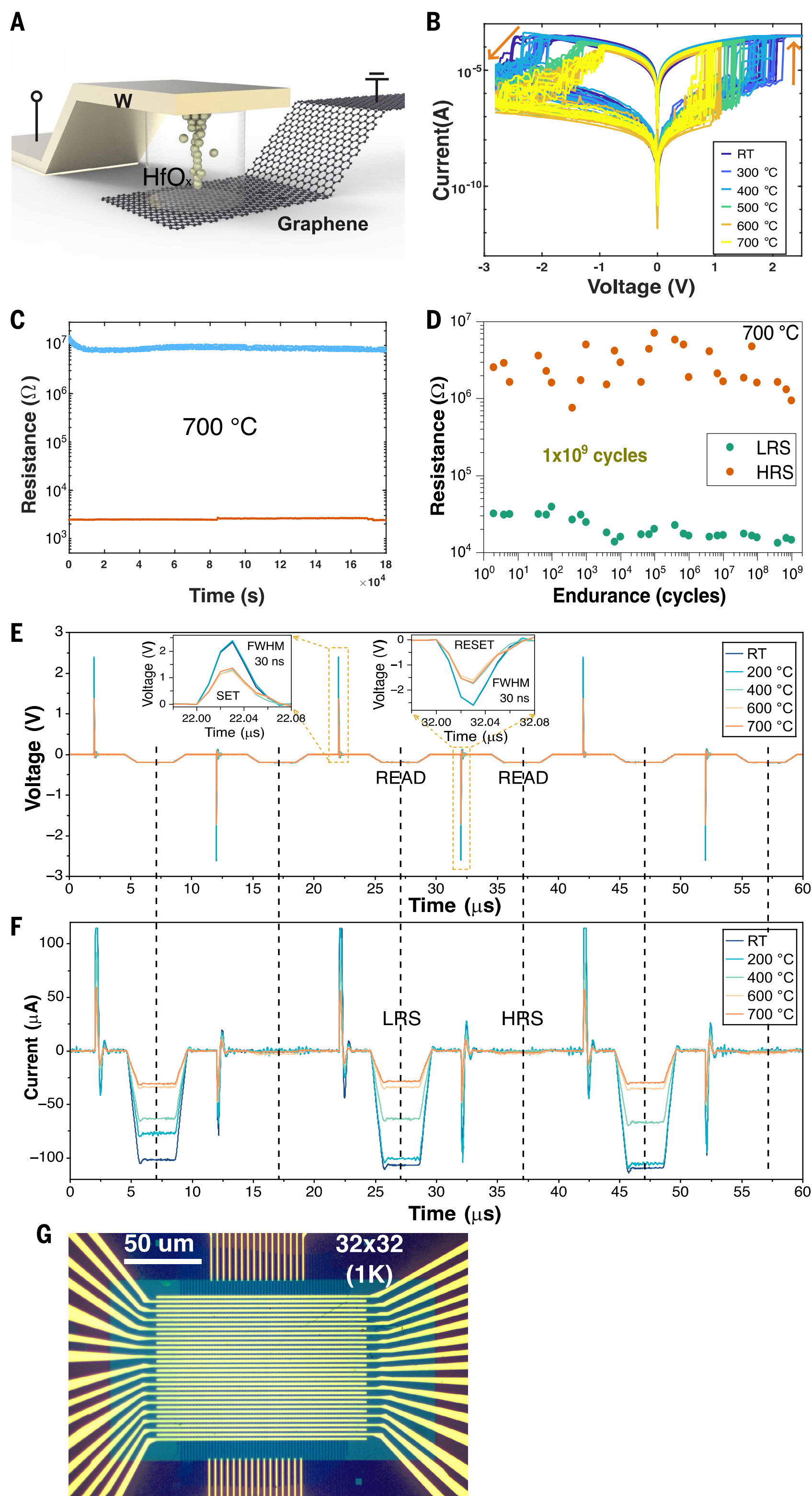

Fig. 1. Schematic and high-temperature performance of Gra/HfO$_x$/W devices. (**A**) Schematic drawing of the Gra/HfO$_x$/W device. (**B**) dc *I*-*V* switching curves of Gra/HfO$_x$/W devices measured in situ at various temperatures. (**C**) In situ retention data of Gra/HfO$_x$/W devices at 700°C. (**D**) In situ writing endurance data of Gra/HfO$_x$/W devices at 700°C. (**E**) Voltage waveform and (**F**) current response in three continuous pulse switching cycles for the same Gra/HfO$_x$/W device at various temperatures. FWHM pulse widths for both SET and RESET are ~30 ns. The pulse width for READ is 5 μs, and the reading voltage is 0.2 V. (**G**) Optical image of a 32 by 32 (1K) crossbar array based on Gra/HfO$_x$/W devices by using a two-wire configuration. Each device cell has a footprint of ~1 μm by 1 μm.

cycles of the Gra/HfO$_x$/W device at 700°C. During the electrical measurements, the bottom Gra electrode was grounded, and a bias voltage was applied to the top W electrode. The switching polarity was dictated by the relative electrochemical reactivity of the two electrodes. According to the Ellingham diagram (*26*, *27*), W exhibits a higher reactivity toward oxygen (O) than carbon in the temperature range of interest, designating W as the active electrode and Gra as the inert one. When a positive bias was applied, the W electrode underwent oxidation, extracting O from the HfO$_x$ layer and generating O vacancies near the W/HfO$_x$ interface, which is consistent with the valence change mechanism commonly observed in oxide memristors (*28*–*35*). The applied field then drove these positively charged O vacancies toward the inert counter electrode, where their accumulation forms conductive filaments, switching the device into the ON state (SET). Applying a reverse bias resulted in the rupture of these filaments, likely driven by the combined effects of the electric field and joule heating, restoring the device to the OFF state (RESET). Notably, 700°C represents the upper limit of our in situ high-temperature probe station, not the operational limit of the Gra/HfO$_x$/W devices.

During quasi-dc switching measurements at temperatures ranging from RT to 700°C, the device consistently maintained an ON/OFF current ratio of approximately three orders of magnitude. Across this temperature range, the SET transitions remained abrupt, and the RESET transitions evolved from abrupt to more gradual behavior toward higher temperatures. Additionally, the SET threshold voltage decreased progressively from 2 V at RT to 1 V at 700°C, and the peak RESET current dropped from 300 to 100 μA with increasing temperature. These trends indicate that the switching process gradually becomes easier at elevated temperatures, which is consistent with the thermally assisted nature of filament formation and rupture. Additionally, the results suggest that higher operating temperatures could help reduce the energy consumption of memristor devices.

We further evaluated the thermal stability of Gra/HfO$_x$/W devices at elevated temperatures, focusing on data retention and write endurance. The in situ retention characteristics of both ON and OFF states at 700°C are shown in Fig. 1C. To minimize disturbance to the memory states, a low read voltage of 50 mV, which is well below the SET and RESET thresholds, was applied, and resistance values were sampled every 10 s. During the 50-hour retention test, no substantial resistance drift was observed in either state, and the memory window remained above three orders of magnitude without any refreshing. With periodic refreshing, typically used in dynamic random-access memory, the operational stability could be further enhanced. The ON state remained stable throughout the entire test, and the OFF state showed a minor initial resistance drop, likely owing to complete crystallization of the HfO$_x$ layer. To assess the device-to-device variation in high-temperature retention, we conducted annealing tests on 30 Gra/HfO$_x$/W devices at 700°C, as shown in fig. S2. The average retention time for both ON and OFF states

Downloaded from https://www.science.org at University of Southern California on May 22, 2026

was ~145 hours, with individual devices exhibiting retention time ranging from 130 to 170 hours. In addition, we evaluated the reading disturbance immunity by performing in situ reading endurance tests on our Gra/HfO_x/W devices at 700°C (fig. S3). Both ON and OFF states remained stable without noticeable disturbance for at least 10^9 reading cycles at V_{read} = 0.5 V, indicating excellent robustness against reading disturbance even under extreme-temperature operation.

The in situ writing endurance performance of the Gra/HfO_x/W device at 700°C under pulse switching is shown in Fig. 1D. We used a write-and-verify protocol, with a fixed pulse width of 1 μs for both SET and RESET operations. The READ pulse was fixed at 0.5 V with a duration of 10 μs (fig. S4). The device sustained more than 10^9 switching cycles and maintained an ON/OFF current ratio of approximately two orders of magnitude at 700°C driven by an open-loop circuit under fixed switching operation conditions. The pulse amplitude and width were intentionally kept moderate to ensure stable cycling, which results in a smaller ON/OFF current ratio than that observed in dc measurements. The device retained full switching functionality even after 10^9 cycles. To further evaluate device-to-device variation in high-temperature endurance, we measured the in situ pulse switching performance of eight individual devices. Most of them exhibited excellent endurance, ranging from 100 million to 1 billion switching cycles at 700°C (fig. S5). Excellent cycle-to-cycle repeatability and a stable memory window were maintained even at 700°C, demonstrating the strong potential of Gra/HfO_x/W devices for high-density memory and computing applications in extreme thermal environments. After an excessive number of switching cycles, some of our Gra/HfO_x/W devices eventually became permanently stuck in the ON state. This endurance failure was attributed to O loss during repeated cycling, a mechanism that is consistent with conventional HfO_x-based memristors. For high-temperature retention tests, degradation was likewise dominated by drift from the high-resistance state (HRS) to the low-resistance state (LRS) but driven by the diffusion of active electrode (W here). This pathway was strongly suppressed, though not eliminated, by our Gra/HfO_x interfacial design. With prolonged annealing at high temperature, additional W can gradually enter the HfO_x layer and approach the Gra/HfO_x interface, eventually leading to failure.

We also investigated the effect of temperature on the switching dynamics of the Gra/HfO_x/W device. The input voltage waveforms during three consecutive switching cycles are shown in Fig. 1E, and the corresponding output current waveforms recorded from RT to 700°C are shown in Fig. 1F. The full width at half maximum (FWHM) of both SET and RESET pulses was ~30 ns. For READ operations, a fixed pulse voltage of 0.2 V and a pulse width of 5 μs were used. The SET and RESET pulse voltages were around 2.5 V at RT and 200°C, decreasing to ~1.5 V at 400°C and above, which is consistent with the trends observed in quasi-dc switching measurements. By comparing the read currents before and after each SET/RESET pulse, we confirmed that the device could be successfully switched between different resistance states by using 30-ns-wide pulses. The pulse switching voltage was relatively small, and switching speed has potential for further improvement at higher pulse voltages. The measured switching time was presently constrained by parasitic capacitance in the test circuitry, rather than the intrinsic switching speed of the device.

For the effective utilization of Gra/HfO_x/W devices in high-temperature applications, multistate capability and linear *I-V* characteristics are highly desirable. We successfully programmed our Gra/HfO_x/W devices into 32 distinct resistance states at 700°C, with their corresponding *I-V* responses remaining reasonably linear at this elevated temperature (figs. S6 and S7). The quantitative correlation coefficients for 16 representative resistance states all exceeded 0.995 over the 0 to 0.5 V range, demonstrating excellent Ohmic-like linearity. These results confirmed the strong potential of our devices for high-temperature multilevel memory and in-memory computing applications.

To evaluate the feasibility of large-scale integration of Gra/HfO_x/W devices, we fabricated a 32 by 32 (1K) crossbar array using a two-wire configuration (Fig. 1G). Because of the absence of selector elements, our testing focused on the diagonal devices in the 1R crossbar array. The dc switching characteristics of these devices are presented in fig. S8. After the electroforming process, six devices became stuck in the ON state. However, all remaining devices exhibited stable and repeatable RS behavior, with ON/OFF current ratios exceeding three orders of magnitude. This result corresponds to a device yield of 81.25% in the first fabricated array of this kind. This yield is substantially greater than that of early-stage conventional memristor arrays, demonstrating promising device uniformity and scalability. These results provide a solid foundation for further upscaling toward larger crossbar arrays for practical applications.

Experimental study of mechanism with TEM

To elucidate the role of Gra in the Gra/HfO_x/W device, we conducted control experiments using Pt/HfO_x/W structures. After annealing at 800°C for 10^4 s under a vacuum of ~10^{-7} torr, the HRS in Pt/HfO_x/W devices quickly degraded into a permanent ON state (Fig. 2A). By contrast, both the HRS and LRS in Gra/HfO_x/W devices remained relatively stable under identical annealing conditions (Fig. 2D). Moreover, the Gra/HfO_x/W devices retained their switching functionality after annealing, with the ON/OFF current ratio remaining largely unchanged (fig. S9). From the comparison between these two types of devices, we found that high temperature–induced failure was predominantly associated with HRS degradation, which typically manifested as a permanent transition to the ON state. This behavior was attributed to W diffusion, as supported by our subsequent experimental and theoretical investigations. A similar HRS-to-LRS failure mode was previously reported in Ta/HfO_x/Pt memristors (*36*), suggesting a broader relevance of this degradation mechanism in oxide-based memristors with reactive electrodes.

Although the suppression of W diffusion was critical for achieving high-temperature reliability, as demonstrated by our Gra/HfO_x design, we also addressed why the LRS exhibited such extraordinary thermal stability. By analyzing the failure time of the HRS at various temperatures, we extracted an effective activation energy for W diffusion in the HfO_x layer to be ~1.82 eV (fig. S10). This value is higher than the reported activation energy of ~1.5 eV for V_O diffusion in HfO_x (*37*), which would suggest that the LRS should degrade more quickly than the HRS at elevated temperatures. However, our experimental results revealed the opposite: The LRS demonstrated substantially longer retention time, with some devices showing no observable degradation even after prolonged annealing at high temperature. This apparent contradiction implied that simple V_O diffusion alone could not account for the high thermal stability of the LRS in our Gra/HfO_x/W devices. Instead, we attributed the LRS stability to a compositional phase separation mechanism proposed recently (*38*), in which Li *et al.* have experimentally demonstrated such phase separation in TaO_x and HfO_x systems during thermal annealing (we discuss further details in the supplementary materials). This thermodynamically driven phase separation leads to the formation of a stable, persistent interface between O-rich and O-deficient regions (*39*), which can effectively suppress long-range V_O migration and thereby stabilize the conductive filament. Although direct observation of such filaments or phase-separated structures remains challenging, we provided indirect evidence supporting the existence of a V_O-rich filament by analyzing the spatial distribution of V_O (fig. S11).

We also explored alternative top-electrode materials (Ru, Pt, and Ta) in addition to W. Under identical annealing conditions (800°C for 10^4 s), none of these alternatives maintained a stable HRS; all devices showed an abrupt HRS-to-LRS transition at the first measurement point (1800 s) (fig. S12). Specifically, Gra/HfO_x/Ru and Gra/HfO_x/Pt devices became irreversibly stuck ON after annealing, whereas Gra/HfO_x/Ta devices could

Downloaded from https://www.science.org at University of Southern California on May 22, 2026

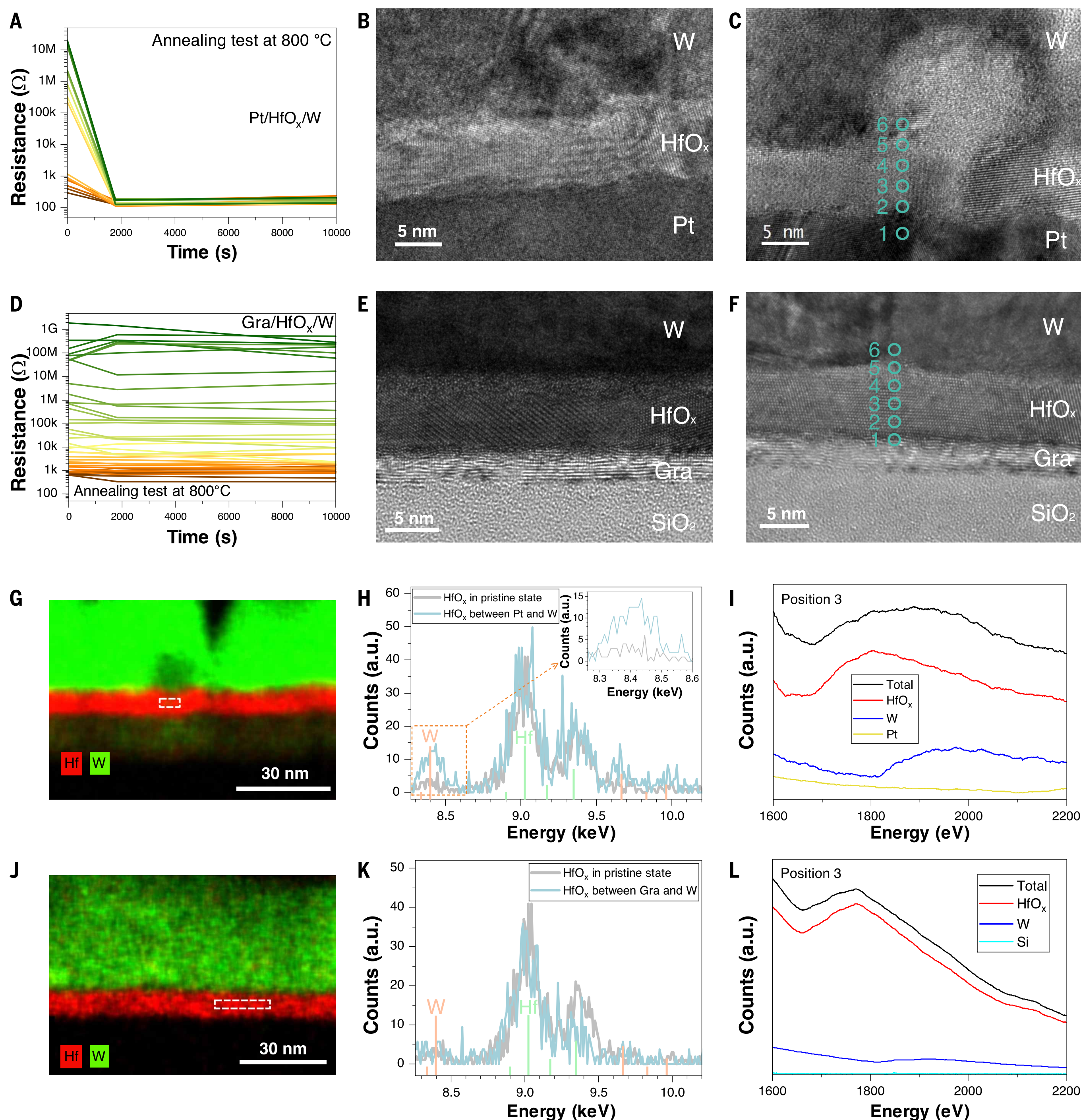

Fig. 2. Mechanism study by means of HRTEM, EDS, and EELS. (**A**) Result of annealing tests for Pt/HfO$_x$/W control devices. All Pt/HfO$_x$/W devices exhibited an abrupt HRS-to-LRS transition at the first testing point (after 1800 s of annealing). (**B** and **C**) Cross-sectional HRTEM images of (B) a Pt/HfO$_x$/W device without annealing and (C) a Pt/HfO$_x$/W device that has been annealed, showing a rough interface between the HfO$_x$ layer and both the top and bottom electrodes. (**D**) Result of annealing tests for Gra/HfO$_x$/W devices. All Gra/HfO$_x$/W devices maintained relatively stable resistance states throughout the entire 10^4 s annealing process. (**E** and **F**) Cross-sectional HRTEM images of (E) a Gra/HfO$_x$/W device without annealing and (F) a Gra/HfO$_x$/W device that has been annealed, highlighting the preserved sharp interfaces. (**G**) EDS mapping of Hf and W elements, (**H**) comparison of EDS spectra between HfO$_x$ inside the device region and pristine HfO$_x$, and (**I**) EELS result at position 3 for a Pt/HfO$_x$/W device that has been annealed, confirming the W presence inside the HfO$_x$ layer. (**J**) EDS mapping of Hf and W elements, (**K**) comparison of EDS spectra between HfO$_x$ inside the device region and pristine HfO$_x$, and (**L**) EELS result at position 3 for a Gra/HfO$_x$/W device that has been annealed, confirming the negligible W signal in the HfO$_x$ layer. The MLLS technique was used to determine the signal of individual elements in EELS analysis, in which reference spectra with appropriate weights are summed linearly to fit the experimental spectra. The weights of each component were determined by minimizing the difference between the model-fitted and experimental spectra according to the least-squares principle. The EDS comparison in (G) and (J) was performed by normalizing the spectra to the integrated counts of the Hf peak.

Downloaded from https://www.science.org at University of Southern California on May 22, 2026

still be switched back to the HRS. This trend was consistent with the melting points (Pt, 1770°C; Ru, 2334°C; Ta, 3017°C; and W, 3422°C): Metals with lower melting points generally have increased atomic mobility at elevated temperatures, accelerating diffusion-driven degradation.

Next, we examined and compared the microstructure and elemental distribution of both Gra/HfO_x/W and Pt/HfO_x/W devices with and without high-temperature annealing. All devices were electroformed before the high-temperature annealing. Without annealing, the cross-sectional HRTEM image of the Pt/HfO_x/W device (Fig. 2B) revealed a rough interface between the HfO_x layer and both the top and bottom electrodes, which is a feature frequently observed in bulk memristors. By contrast, the Gra/HfO_x/W device exhibited sharp, well-defined interfaces between the HfO_x layer and the adjacent electrodes (Fig. 2E). This improved interfacial quality was attributed to the atomically flat surface, chemical inertness, and impermeable nature of Gra (*40*), which together helped preserve the structural integrity of the device. The deposition of HfO_x on Gra resulted in a much smoother film, primarily owing to the absence of nucleation sites and the low initial surface diffusivity of adatoms (*41*), which suppressed the formation of large islands. As a result, the top surface of the HfO_x layer remained relatively smooth, yielding a substantially flatter HfO_x/W interface compared with devices with a Pt bottom electrode. This enhanced flatness of the HfO_x/W interface is expected to yield much more uniform electrical properties, with fewer defects propagating through HfO_x, and to enhance thermal and structural stability by minimizing the interfacial area. In conventional metal-insulator-metal memristors produced through techniques such as magnetron sputtering or e-beam evaporation, realizing such interface uniformity remains a major challenge (*16*).

For samples annealed at 800°C, the cross-sectional HRTEM image of the Pt/HfO_x/W device (Fig. 2C) exhibited a bright-contrast protrusion like a mushroom, extending from the HfO_x/W interface into the W electrode. Further examination by means of EDS and EELS using high-angle annular dark-field scanning TEM (HAADF-STEM) confirmed that this feature had a lower average atomic number (Z) because of a higher oxygen concentration than the surrounding W layer (fig. S13), suggesting the formation of tungsten oxide (WO_x). An examination of HfO_x beneath the mushroom-like feature clearly showed an amorphous grain boundary, which was likely to act as conduction pathways of ions. By contrast, the cross-sectional HRTEM images of the Gra/HfO_x/W device annealed at 800°C (Fig. 2F) showed that the Gra/HfO_x interface remained sharp, although some roughening was observed at the HfO_x/W interface compared with the pre-annealing state. In addition, we used nanobeam electron diffraction to obtain local diffraction patterns from the thin HfO_x layer inside device region after annealing. Phase identification in this system was inherently challenging because multiple HfO_x polymorphs have similar lattice constants and thus yielded closely spaced diffraction features. This challenge was further compounded by the thin, polycrystalline nature of the HfO_x film and by stress introduced by the top W electrode, both of which could shift the measured d-spacings relative to bulk reference values. Nevertheless, through detailed analysis and comparison with calculated d-spacings, we found that the diffraction data were most consistent with the orthorhombic phase (fig. S14). No mushroom-like features were detected in the W electrode, and the HfO_x layer maintained high crystallinity with no amorphous grain boundaries in the Gra-based devices. Electrochemical migration of O into the W electrode during the forming process could be strongly enhanced by the electric-field concentration effect at rough interfaces. In the Pt/HfO_x/W device, local electric fields could be intensified by up to an order of magnitude at nanoscale protrusions or spikes in the HfO_x film, substantially accelerating O transport into the W layer and potentially leading to the formation of prominent mushroom-like features. We also used atomic force microscopy to quantitatively assess the surface roughness of Pt and Gra (fig. S15). The results confirmed that the Gra electrode exhibited a substantially smoother surface compared with that with Pt, which is consistent with our cross-sectional TEM observations. Furthermore, statistical analysis of the forming voltages for 20 devices of each type (fig. S16) revealed that Pt-based devices were much easier to electroform than their Gra-based counterparts. This difference was likely attributable to variations in surface morphology at the electrode-HfO_x interface, where the rougher Pt surface could locally enhance the electric field and facilitate the electroforming process.

To further investigate the mechanism of thermal stability, we used EDS analysis to compare the elemental distribution in Pt/HfO_x/W and Gra/HfO_x/W devices after annealing. The cross-sectional EDS elemental mapping of Hf and W in the Pt/HfO_x/W device is shown in Fig. 2G. We observed a clear migration of W atoms from the top electrode through the HfO_x layer and into the bottom Pt electrode. Regions closer to the mushroom-like feature exhibited more W migration into the Pt electrode, likely owing to accelerated transport along the conductive path beneath the feature. In Fig. 2H, we compare the EDS spectra of the HfO_x layer between the Pt and W electrodes with those of pristine HfO_x. As a control, pristine HfO_x or Pt outside the device region, where no W electrode was present, should exhibit no W signal, serving as a reference to assess W migration. By examining the characteristic W peak at ~8.4 keV, it was evident that W atoms had migrated into the HfO_x layer after annealing. No noticeable W signal was detected inside the HfO_x layer of electroformed Pt/HfO_x/W devices before annealing (fig. S17), indicating that the W presence in HfO_x originated from diffusion during the annealing process. EDS data from the Pt electrode further confirmed that W had also migrated into the bottom electrode (fig. S18B). Because no substantial electric field could develop across the metallic Pt layer, electric field–driven migration was unlikely; thus, thermal diffusion was the most possible mechanism for W incorporation into the Pt bottom electrode.

By contrast, the EDS elemental maps of Hf and W in the Gra/HfO_x/W device are presented in Fig. 2J. We observed no noticeable W diffusion into the Gra electrode, highlighting the excellent impermeability of Gra. In Fig. 2K, we compare the EDS spectra of the HfO_x layer between the Gra and W electrodes with those of pristine HfO_x. The W peak at ~8.4 keV was barely detectable, indicating that W diffusion into the HfO_x layer was also negligible. This explained the preserved resistance states and robust switching behavior of the Gra/HfO_x/W device at high temperatures and suggested that the switching mechanism was dominated by the migration of oxygen vacancies rather than W. EDS analysis of the Gra electrode also confirmed the absence of W diffusion (fig. S18D). To further improve spatial coverage and reduce the possibility that localized diffusion outside the initially examined region was overlooked, we repeated cross-sectional TEM/EDS studies on multiple Gra/HfO_x/W devices with dimensions of 1 μm by 300 nm. To mitigate probe broadening, the samples were thinned along the shorter device dimension to ~30 nm, as measured with EELS. EDS measurements were then acquired across the entire device along the 1-μm lateral direction, in sequential subsections spanning 100 nm each. Despite this comprehensive spatial coverage, we did not observe any pronounced W diffusion in the Gra/HfO_x/W devices after annealing (fig. S19).

Furthermore, we used STEM-EELS analysis to examine W diffusion into the RS layer after annealing. We used multiple linear least squares (MLLS) technique (*42*, *43*) to determine the signal of Hf, W, and Pt, in which reference spectra with appropriate weights were summed linearly to fit the experimental spectra. The reference spectrum for Hf was obtained from pristine HfO_x well outside the device region, whereas those for W and Pt were extracted from the electrode regions far from the dielectric-electrode interface (fig. S20A). The weights of each component were determined by minimizing the difference between the model-fitted and experimental spectra according to the least-squares principle. The EELS spectrum acquired at position 3 in

Downloaded from https://www.science.org at University of Southern California on May 22, 2026

the Pt/HfO_x/W device is shown in Fig. 2I (EELS data from points 1 to 6, spanning from the Pt bottom electrode through the HfO_x layer to the W top electrode, are provided in fig. S20B). A pronounced W signal was detected in the middle of the HfO_x layer and even at the Pt/HfO_x interface (position 2), indicating that W atoms penetrated across the HfO_x layer and reached the Pt bottom electrode. These findings are consistent with the irreversible transition to the ON state observed in Pt/HfO_x/W devices after high-temperature annealing.

By contrast, the EELS result at position 3 inside the Gra/HfO_x/W device is shown in Fig. 2L (EELS data from points 1 to 6, covering regions from the Gra electrode through the HfO_x layer to the W top electrode, are shown in fig. S20C). No appreciable W signal was observed in the middle of the HfO_x layer. Instead, W was detected only at points 4, 5, and 6, corresponding to the HfO_x surface and the W layer, whereas positions 1, 2, and 3 showed no meaningful W signal. This result confirmed that W diffusion in the Gra/HfO_x/W device was confined to the top surface of the HfO_x layer and did not penetrate through the switching layer. These results indicate that the switching mechanisms in both Pt/HfO_x/W and Gra/HfO_x/W devices were primarily governed by electric field–driven migration of O vacancies. From RT to 700°C, the ON state of our Gra/HfO_x/W device showed Ohmic-like *I-V* characteristics up to 0.5 V with a positive but very small temperature coefficient of resistance (TCR) of ~8.2×10^{-5} K^{-1} (fig. S21). This value was far below the bulk TCR of W (~4.5×10^{-3} K^{-1}), suggesting that the filament was unlikely to be W. However, the failure of the Pt/HfO_x/W device was attributed to the thermal diffusion of W atoms, which penetrated through the thin HfO_x layer and agglomerated on the Pt electrode, ultimately leading to device shorting. Although W diffusion could also occur in Gra/HfO_x/W devices at high temperatures, W atoms did not readily agglomerate or grow on the Gra electrode. This feature inhibited filament overgrowth, preserving switching functionality and preventing device failure. Because of the detection limits of EELS/EDS, we could not determine whether the equilibrium W concentration in HfO_x was strictly zero in annealed Gra/HfO_x/W devices. However, we confirmed that the W incorporation into HfO_x was substantially lower in Gra-based devices than in Pt control devices under identical annealing conditions. This agreed with the very low equilibrium solubility of W in HfO_2. A detectable signal requires a separate W-rich phase beyond a critical size in the HfO_2 matrix, which was promoted by Pt but suppressed by Gra.

Theoretical study by means of first-principles calculation

To understand the experimental observations regarding thermal stability, we performed first-principles calculations of W adatoms on Pt and Gra surfaces. In Fig. 3A, we summarize the calculated adsorption energies for W adatoms and dimers, along with the corresponding diffusion coefficients on Pt (111) and Gra surfaces. Detailed analyses of the stable and metastable adsorption sites on the Pt (111) and Gra surfaces are provided in figs. S22 to S25. On the Pt (111) surface, the adsorption energy of a single W adatom was −9.08 eV at the most stable site and −8.92 eV at a nearby metastable site, indicating strong binding between W and Pt. By contrast, on the Gra surface the adsorption energy was markedly lower in magnitude, with −2.80 eV at the most stable site and −1.84 eV at a metastable site. These results suggest a substantially weaker interaction between W and Gra, which is consistent with the scenario that Gra served as a chemically inert, thermally robust barrier that inhibited filament nucleation and metal diffusion.

To further assess the interaction between multiple W atoms, we calculated the adsorption energy of W dimers and found an even more pronounced difference between the Pt (111) and Gra surfaces. On the Pt (111) surface, the adsorption energy of a W dimer was −4.81 eV for

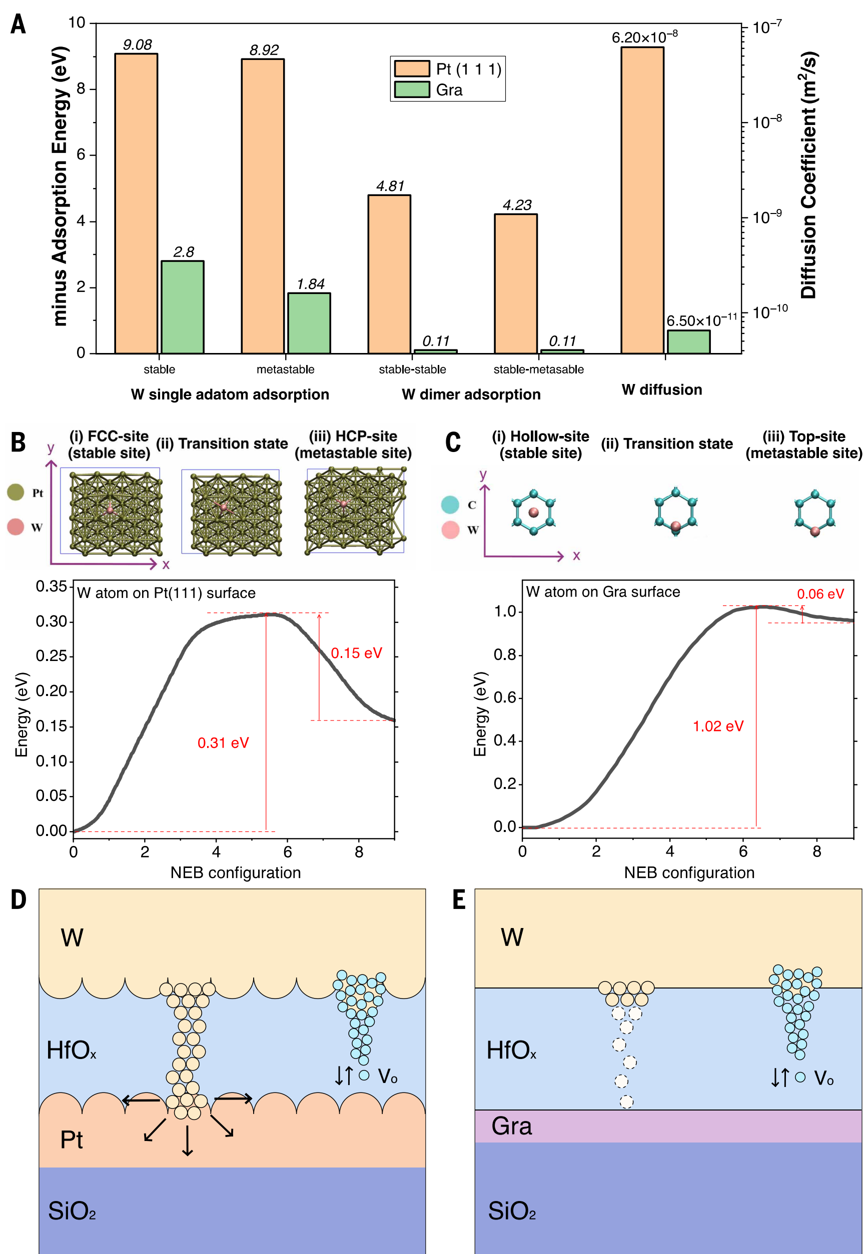

Fig. 3. Mechanism study by means of first-principles calculation. (**A**) Calculated adsorption energies of W single adatom and dimer, as well as the diffusion coefficients of W on Pt(111) and Gra surfaces. (**B** and **C**) Atomic configurations of a W atom at the stable site, transition state, and metastable site on the (B) Pt(111) surface and (C) Gra surface, as well as the energy profile along the NEB path. FCC, face-centered cubic; HCP, hexagonal close-packed. (**D** and **E**) Schematic diagrams illustrating the resistance switching mechanism and thermal diffusion of W in (D) Pt/HfO_x/W and (E) Gra/HfO_x/W devices.

Downloaded from https://www.science.org at University of Southern California on May 22, 2026

adjacent stable–stable sites and −4.23 eV for adjacent stable–metastable sites. By contrast, on the Gra surface, the adsorption energy for the W dimer was nearly zero, ~−0.11 eV, for both stable-stable and stable-metastable configurations. This result suggests that W dimers were weakly bound on the Gra surface and could easily desorb at elevated temperatures, making cluster formation on Gra energetically unfavorable. These results clearly demonstrated that both single W adatoms and dimers bound much more strongly to Pt than to Gra at both stable and metastable sites. The markedly more negative adsorption energies on Pt imply that W adatoms were less likely to desorb, favoring their aggregation into clusters and conductive filaments. Conversely, the weak binding on Gra surfaces suppressed W accumulation and filament nucleation.

The simulations were performed on idealized, atomically flat Pt and Gra surfaces. In practice, Pt exhibited a much rougher surface than Gra, as confirmed with cross-sectional HRTEM images. This increased roughness could further enhance surface adsorption by increasing the effective surface area and creating diverse adsorption sites, including steps, kinks, and other surface defects (*44*, *45*). These morphological features were likely to further amplify the contrast between Pt and Gra surfaces in terms of W adsorption, reinforcing the role of Pt as a much more effective sink for W atoms compared with Gra.

To evaluate the mobility of W adatoms and their potential to form clusters, we computed the activation energy barriers and diffusion coefficients for W atom migration on the Pt (111) and Gra surfaces. Filament formation required that W adatoms migrate across the electrode surface and coalesce into metallic clusters. Using the nudged elastic band (NEB) method (*46*), we calculated the minimum energy paths and the corresponding activation energy barriers (E_B) for W atom migration between stable and metastable sites. According to transition-state theory (*47*), higher activation barriers correlate with lower adatom diffusivity.

The atomic configurations and energy profile for a W adatom migrating on the Pt (111) surface are given in Fig. 3B. The activation energy barrier was found to be 0.30 eV from the stable to the metastable site and 0.15 eV in the reverse direction. The corresponding NEB results for W migration on the Gra surface are shown in Fig. 3C. In this case, the activation barriers were 1.02 eV (stable to metastable) and 0.06 eV (metastable to stable). These values indicate that the average energy barrier for W adatom diffusion on Gra was substantially higher than on Pt (111).

To migrate between two adjacent stable sites, a W adatom must sequentially overcome both E_{B1} (stable → metastable) and E_{B2} (metastable → stable). Using these barriers, we computed the surface diffusion

Downloaded from https://www.science.org at University of Southern California on May 22, 2026

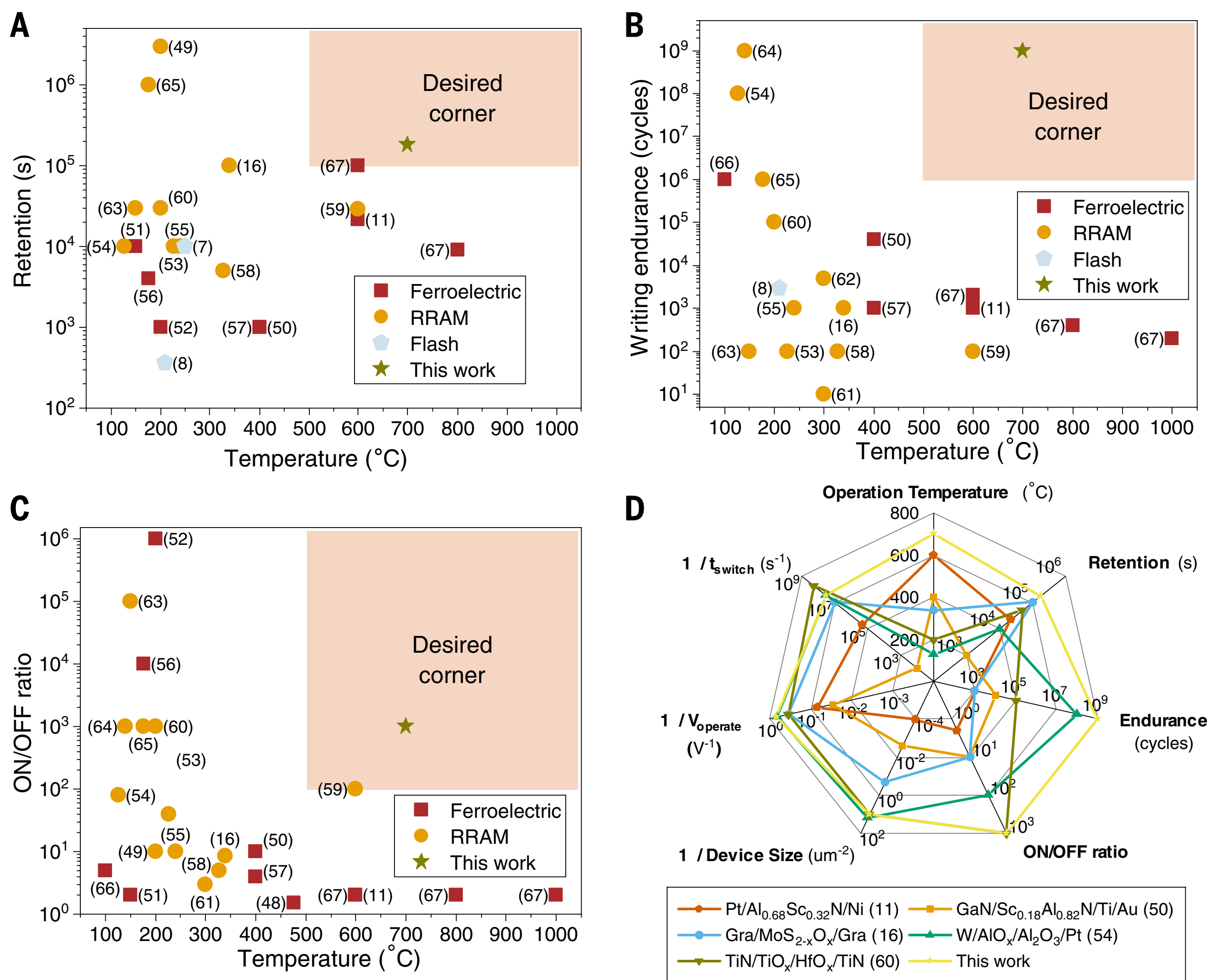

Fig. 4. Benchmark of high-temperature NVM technologies. (**A**) Data retention as a function of operation temperature. (**B**) Writing endurance as a function of temperature. (**C**) ON/OFF current ratio as a function of temperature. (**D**) Comparison among some typical high-temperature resistive NVMs in terms of operation temperature, switching pulse width and voltage, device size, ON/OFF current ratio, writing endurance, and data retention. RRAM, resistive random-access memory.

coefficients (D), summarized in the rightmost columns of Fig. 3A. The diffusion coefficient of a W adatom on Pt (111) was approximately three orders of magnitude greater than that on Gra. These results confirmed that W atoms diffused far more readily on the Pt surface than on Gra, which is an initially counterintuitive finding, given the stronger W–Pt binding. This enhanced diffusion on Pt (111) could be attributed to the relatively smooth and delocalized electron charge density distribution on its surface (fig. S26), which lowered the diffusion barrier and facilitated adatom mobility.

Initially, we performed our density functional theory (DFT) simulations using a single-layer Gra model. However, cross-sectional TEM images revealed that the actual devices used multilayer Gra as the bottom electrode. To address the potential impact of Gra thickness on W adsorption and diffusion, we extended our DFT calculations to include both bilayer and trilayer Gra configurations. The corresponding results are presented in fig. S27. Comparison of the computed adsorption energies and diffusion barriers for W adatoms on 1L–3L Gra showed negligible variation with increasing layer number. This insensitivity to Gra thickness contrasted with Pt, where adsorption was substantially stronger and diffusion was faster. Our findings indicate that W adsorption remained weak and surface diffusion was intrinsically slow on Gra, regardless of its thickness. These theoretical results were consistent with our experimental observations and reinforced the proposed mechanistic interpretation.

On the basis of the combined results from TEM observations and first-principles calculations, we proposed a mechanistic scenario to explain the superior thermal stability of Gra/HfO_x/W devices compared with their Pt/HfO_x/W counterparts. The Pt/HfO_x/W device exhibited a rough interface between HfO_x and Pt (Fig. 3D). During high-temperature annealing, additional W atoms from the top electrode readily diffused toward the Pt bottom electrode, which effectively served as a sink for W atoms, removing them from the HfO_x film and enabling more atoms to dissolve from the W electrode. This process was strongly accelerated by the large negative adsorption energy of W on Pt. Furthermore, the rough Pt/HfO_x interface increased the effective surface area of the bottom electrode and offered more adsorption sites, facilitating W adsorption. On reaching the Pt surface, the W atoms readily agglomerated and spread across the HfO_x film because of the low diffusion barrier on Pt. As a result, the top and bottom electrodes were quickly connected, rendering the device permanently stuck in the ON state and ultimately leading to irreversible device failure.

By contrast, the Gra/HfO_x/W device features an atomically sharp interface between the HfO_x and Gra layers (Fig. 3E). During high-temperature annealing, W atoms from the top electrode might still diffuse toward the bottom Gra electrode. However, the process was substantially slower than in the Pt-based device because the HfO_x film was saturated with W atoms, and no further dissolution from the W electrode occurred owing to the near-zero adsorption energy of W on Gra. The weak W–Gra interaction, combined with the low surface diffusivity of W on Gra, made it energetically unfavorable for W atoms to attach to or grow on the Gra surface. Additionally, the atomically sharp Gra/HfO_x interface minimized the electrode's surface area and reduced the number of available adsorption sites, further suppressing W adsorption. Consequently, electrical separation between the two electrodes was preserved for a much longer duration, maintaining the device's switching ability. This mechanism explains why the Gra/HfO_x/W device exhibited repeatable switching behavior and maintained a stable memory window even at temperatures up to 700°C.

Benchmark of high-temperature memories

In Fig. 4, A to C, we benchmark the performance of our Gra/HfO_x/W device against previously reported high-temperature NVMs (*7*, *8*, *11*, *16*, *48*–*67*), focusing on operating temperature, retention time, write endurance, and ON/OFF current ratio. To the best of our knowledge, our device demonstrated the highest reported operating temperature among all resistive NVMs, achieving stable performance at 700°C with a retention time of 50 hours without refreshing. This result substantially outperforms other reported devices operating above 250°C. The device also demonstrated exceptional write endurance, exceeding 10^9 cycles at 700°C, representing the highest endurance reported to date for any nonvolatile memory designed for high-temperature operation. To our knowledge, only one other device, operating at 140°C, has shown comparable endurance. By contrast, this endurance surpasses that of NVMs stable above 250°C by more than four orders of magnitude and exceeds those functioning above 600°C by approximately six orders of magnitude. The ON/OFF current ratio remained above three orders of magnitude at 700°C, approximately one order higher than any other high-temperature NVMs reliably operating above 300°C.

In Fig. 4D, we offer a detailed comparison with representative high-temperature resistive NVMs in terms of operating temperature, retention, write endurance, device size, ON/OFF current ratio, switching voltage, and speed (*11*, *16*, *50*, *54*, *60*). Our device showed comprehensive advantages in terms of operating temperature, write endurance, and retention time. Only one device operating below 400°C (*16*) shows a comparable, though still shorter, retention time. The ON/OFF current ratio of our device was higher than that of all other devices at elevated temperatures, except for one device operating at 200°C (*60*), which shows a similar memory window. Our device also maintained a low operation voltage (~1.5 V), short switching pulse (~30 ns), and a compact size (<1 μm^2).

The results of annealing tests at 800°C suggest that 700°C is not the intrinsic operating limit of the Gra/HfO_x/W device but rather a limitation imposed by our measurement setup.

Conclusions

We have demonstrated a type of bipolar memristor based on Gra/HfO_x/W structures that exhibited exceptional high-temperature performance. The devices reliably operated at 700°C, achieving a stable ON/OFF current ratio of three orders of magnitude. At this temperature, they maintained ON and OFF states for more than 50 hours without refreshing and endured at least 10^9 switching cycles. The devices operated at ~1.5 V and could be switched by using 30-ns-wide pulses at 700°C.

Physical characterization revealed that for Pt/HfO_x/W devices, W atoms diffused through HfO_x and into the bottom Pt electrode after annealing at 800°C, leading to irreversible conductive states. By contrast, no noticeable W diffusion into HfO_x or onto the bottom Gra electrode was observed in the Gra/HfO_x/W devices. These observations can be understood through our theoretical study, which showed that W atoms bound more strongly and diffused more readily on Pt (111) surfaces compared with Gra because of more negative adsorption energies and smaller diffusion barriers.

Our findings push the boundaries of high-temperature memristor performance and open new avenues for developing thermally robust memristive devices, which have become increasingly important in the era of space exploration.

REFERENCES AND NOTES

1. V. E. Chelnokov, A. L. Syrkin, *Mater. Sci. Eng. B* **46**, 248–253 (1997).
2. P. G. Neudeck, D. J. Spry, L. Chen, N. F. Prokop, M. J. Krasowski, *IEEE Electron Device Lett.* **38**, 1082–1085 (2017).
3. TTSemiconductor, "Memory and general purpose products for high temperature, harsh environments"; https://ttsemiconductor.com/Memory-Products-For-High-Temperature-Harsh-Environments-1003-295.html (accessed 11 Jun 2025).
4. D. K. Pradhan *et al.*, *Nat. Rev. Mater.* **9**, 790–807 (2024).
5. E. Prokhorov, G. Trapaga, J. González-Hernández, *J. Appl. Phys.* **104**, 103712 (2008).
6. M. Le Gallo, A. Sebastian, *J. Phys. D Appl. Phys.* **53**, 213002 (2020).
7. B. Govoreanu, J. Van Houdt, *IEEE Electron Device Lett.* **29**, 177–179 (2008).
8. K. Lee *et al.*, *IEEE Trans. Electron Dev.* **60**, 1099–1107 (2013).
9. K. Lee *et al.*, *IEEE Electron Device Lett.* **34**, 48–50 (2013).

Downloaded from https://www.science.org at University of Southern California on May 22, 2026

10. M. C. Morgul, M. N. Sakib, M. Stan, "Reliable processing in flash with high temperature," in *2021 IEEE International Integrated Reliability Workshop (IIRW)* (2021); https://dx.doi.org/10.1109/IIRW53245.2021.9635624.
11. D. K. Pradhan *et al.*, *Nat. Electron.* **7**, 348–355 (2024).
12. W. Zhang *et al.*, *Science* **381**, 1205–1211 (2023).
13. T.-H. Wen *et al.*, *Science* **384**, 325–332 (2024).
14. J. Li *et al.*, *Sci. Adv.* **9**, eadf7474 (2023).
15. Y. Lu *et al.*, *Adv. Intell. Syst.* **7**, 2401068 (2025).
16. M. Wang *et al.*, *Nat. Electron.* **1**, 130–136 (2018).
17. C. Pan *et al.*, *Adv. Funct. Mater.* **27**, 1604811 (2017).
18. W. Wang, C. Wu, Z. Li, K. Liu, *Adv. Mater.* **37**, e2418439 (2025).
19. Y. Yang *et al.*, *Adv. Mater.* **26**, 3693–3699 (2014).
20. Y. Shi *et al.*, *Nat. Electron.* **1**, 458–465 (2018).
21. S.-H. Bae *et al.*, *Nat. Mater.* **18**, 550–560 (2019).
22. L. Sun *et al.*, *Sci. Adv.* **7**, eabg1455 (2021).
23. S. Chen *et al.*, *Nat. Electron.* **3**, 638–645 (2020).
24. D. Qi *et al.*, *Adv. Funct. Mater.* **33**, 2301704 (2023).
25. X. Li *et al.*, *Science* **324**, 1312–1314 (2009).
26. B. Pang, Y. Li, Y. Qi, Y. Chen, L. Nan, *J. Mater. Sci.* **60**, 13621–13635 (2025).
27. L. Oar-Arteta, T. Wezendonk, X. Sun, F. Kapteijn, J. Gascon, *Mater. Chem. Front.* **1**, 1709–1745 (2017).
28. R. Zhao *et al.*, *Chem. Rev.* **125**, 745–785 (2025).
29. Z. Wang *et al.*, *Nat. Rev. Mater.* **5**, 173–195 (2020).
30. M. Li *et al.*, *Nat. Electron.* **6**, 491–505 (2023).
31. A. Wedig *et al.*, *Nat. Nanotechnol.* **11**, 67–74 (2016).
32. J. Tang *et al.*, *Adv. Mater.* **31**, e1902761 (2019).
33. M.-K. Song *et al.*, *ACS Nano* **17**, 11994–12039 (2023).
34. Y. Zhong *et al.*, *Nat. Commun.* **12**, 408 (2021).
35. M. Zhao, B. Gao, J. Tang, H. Qian, H. Wu, *Appl. Phys. Rev.* **7**, 011301 (2020).
36. H. Jiang *et al.*, *Sci. Rep.* **6**, 28525 (2016).
37. Y. Y. Chen *et al.*, *IEEE Trans. Electron Dev.* **60**, 1114–1121 (2013).
38. J. Li *et al.*, *Matter* **7**, 3970–3993 (2024).
39. S. J. Kim, J. J. Yang, *Device* **2**, 100625 (2024).
40. Y. Zhao *et al.*, *Small* **10**, 4521–4542 (2014).
41. W. M. Tong, R. S. Williams, *Annu. Rev. Phys. Chem.* **45**, 401–438 (1994).
42. R. F. Egerton, *Electron Energy-Loss Spectroscopy in the Electron Microscope* (Springer, ed. 3, 2011).
43. R. Leapman, *Transmission Electron Energy Loss Spectrometry in Materials Science and The EELS Atlas*, C. C. Ahn, Ed. (Wiley, ed. 2, 2004).
44. S. Zhan *et al.*, *Chem. Eng. J.* **498**, 155322 (2024).
45. B. Yang, H. Suhl, *Phys. Rev. B Condens. Matter* **31**, 614–615 (1985).
46. G. Henkelman, H. Jónsson, *J. Chem. Phys.* **113**, 9978–9985 (2000).
47. D. G. Truhlar, B. C. Garrett, S. J. Klippenstein, *J. Phys. Chem.* **100**, 12771–12800 (1996).
48. P. Wang *et al.*, *Adv. Mater.* **36**, e2400655 (2024).
49. J. R. Jameson *et al.*, in *2013 IEEE International Electron Devices Meeting* (IEEE, 2013), pp. 30.1.1–30.1.4; https://dx.doi.org/10.1109/IEDM.2013.6724721.
50. D. Wang *et al.*, *Adv. Electron. Mater.* **8**, 2200005 (2022).
51. M. Östling, S.-M. Koo, C.-M. Zetterling, S. Khartsev, A. Grishin, *Thin Solid Films* **469– 470**, 444–449 (2004).
52. J. Noh *et al.*, *IEEE Trans. Electron Dev.* **68**, 2515–2521 (2021).
53. G. Khurana, P. Misra, R. S. Katiyar, *J. Appl. Phys.* **114**, 124508 (2013).
54. X.-D. Huang *et al.*, *IEEE Electron Device Lett.* **41**, 549–552 (2020).
55. Z. Liu *et al.*, *ACS Appl. Mater. Interfaces* **13**, 58885–58897 (2021).
56. J. Jiang, X. Chai, C. Wang, A. Jiang, *J. Alloys Compd.* **856**, 158155 (2021).
57. D. Drury, K. Yazawa, A. Zakutayev, B. Hanrahan, G. Brennecka, *Micromachines* **13**, 887 (2022).
58. K. Sato, Y. Hayashi, N. Masaoka, T. Tohei, A. Sakai, *Sci. Rep.* **13**, 1261 (2023).
59. H. Suga *et al.*, *Sci. Rep.* **6**, 34961 (2016).
60. H. Y. Lee *et al*., in *2008 IEEE International Electron Devices Meeting* (2008); https://dx.doi.org/10.1109/IEDM.2008.4796677.
61. J. Zhou *et al.*, *Adv. Mater.* **33**, e2006201 (2021).
62. J. Li *et al.*, *Adv. Mater.* **35**, e2209728 (2023).
63. D. Yang *et al.*, *Adv. Funct. Mater.* **30**, 2004514 (2020).
64. K. A. Campbell, *Microelectronics J.* **59**, 10–14 (2017).
65. L. Sun *et al.*, *Nat. Commun.* **10**, 3161 (2019).
66. X. Yan *et al.*, *Nano Res.* **15**, 9654–9662 (2022).
67. Y. He *et al.*, *Nano Lett.* **25**, 4767–4773 (2025).

ACKNOWLEDGMENTS

Computing resources were partly provided by the US DOE INCITE Program. The authors acknowledge the use of facilities and instrumentation at the AFRL/RX Materials Characterization Facility (MCF), supported by Air Force contract FA2394-23-C-B028. **Funding:** This work was supported by the Air Force Office of Scientific Research (grant FA9550-24-1-0322); the Army Research Office (grants W911NF2120128 and W911NF1810268); the National Science Foundation, Future Manufacturing Program, award NSF 2240407; and the National Science Foundation (grants 2240407 and 2036359). **Author contributions:** Conceptualization: J.Z., J.J.Y. Methodology: J.Z., K.M., A.N., K.S., S.G., P.V., M.H., Q.X., R.S.W. Investigation: J.Z., C.S.J., K.M., C.B., W.S., K.I., K.S., R.Z., Y.X., H.-T.L., S.J.K. Visualization: J.Z., C.S.J., K.M., C.B., W.S., K.I., S.J.K., R.Z. Funding acquisition: J.J.Y., S.G., R.K.K., A.N., A.K.R., N.G. Project administration: J.J.Y., S.G., A.N., R.S.W., N.G. Supervision: J.J.Y., S.G., A.N., R.S.W. Writing – original draft: J.Z., J.J.Y. Writing – review & editing: J.Z., C.S.G., K.M., C.B., W.S., K.I., R.K.K., A.N., K.S., F.S., P.V., A.K.R., S.G., M.H., Q.X., N.G., R.S.W., J.J.Y. **Competing interests:** The other authors declare that they have no competing interests. **Data, code, and materials availability:** All data needed to evaluate the conclusions in the paper are present in the paper and/or the supplementary materials.

License information: Copyright © 2026 the authors, some rights reserved; exclusive licensee American Association for the Advancement of Science. No claim to original US government works. https://www.science.org/about/science-licenses-journal-article-reuse

SUPPLEMENTARY MATERIALS

science.org/doi/10.1126/science.aeb9934
Materials and Methods; Supplementary Text; Figs. S1 to S27; Tables S1 to S3; References (*68–75*); Data S1 to S4; Movie S1

Submitted 3 September 2025; resubmitted 22 January 2026; accepted 11 March 2026; published online 26 March 2026

10.1126/science.aeb9934

Downloaded from https://www.science.org at University of Southern California on May 22, 2026

High-temperature memristors enabled by interfacial engineering

Jian Zhao, Cameron S. Jorgensen, Krishnamurthy Mahalingam, Cynthia Bowers, Wataru Sugimoto, Kai Ito, Seung Ju Kim, Ruoyu Zhao, Yichun Xu, Han-Ting Liao, Rajiv K. Kalia, Aiichiro Nakano, Kohei Shimamura, Fuyuki Shimojo, Priya Vashishta, Ajit K. Roy, Ning Ge, Miao Hu, R. Stanley Williams, Qiangfei Xia, Sabyasachi Ganguli, and J. Joshua Yang

Science **392** (6799), . DOI: 10.1126/science.aeb9934

Editor's summary

Demand for electronics that withstand extreme thermal environments is rising, spanning deep-well drilling, nuclear energy, autonomous systems, and even the surfaces of Venus and Mercury or near spacecraft engines. Although wide-band-gap semiconductors such as silicon carbide enable transistor operation up to 800°C, reliable nonvolatile memories above 300°C remain elusive. Zhao *et al.* introduce memristors operating above 700°C, with more than 109 switching cycles, data retention for over 50 hours, ON/OFF ratios over 1000, switching speeds under 30 nanoseconds, and operating voltages under 1.5 volts. Material characterization and modeling explain this thermal resilience. These results pave the way for robust, high-temperature memory for extreme applications. —Yury Suleymanov

View the article online
https://www.science.org/doi/10.1126/science.aeb9934
Permissions
https://www.science.org/help/reprints-and-permissions

Downloaded from https://www.science.org at University of Southern California on May 22, 2026

Use of this article is subject to the Terms of service

Science (ISSN 1095-9203) is published by the American Association for the Advancement of Science. 1200 New York Avenue NW, Washington, DC 20005. The title *Science* is a registered trademark of AAAS.

Copyright © 2026 The Authors, some rights reserved; exclusive licensee American Association for the Advancement of Science. No claim to original U.S. Government Works